Accepted Manuscript

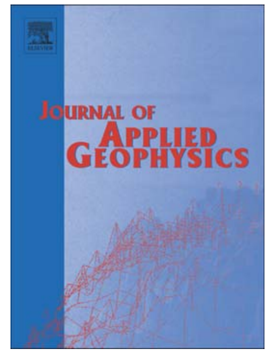

An empirical law for wavelet maxima interpretation of potential fields: Application to the Uinta Mountains range

Paul Cavalier, Alireza Baghai-Wadji, Yohann Poprawski, Michael Inggs

PII: S0926-9851(16)30236-1
DOI: doi: 10.1016/j.jappgeo.2016.08.008
Reference: APPGEO 3054

To appear in: *Journal of Applied Geophysics*

Received date: 4 September 2015
Revised date: 15 July 2016
Accepted date: 23 August 2016

AN EMPIRICAL LAW FOR WAVELET MAXIMA INTERPRETATION OF POTENTIAL FIELDS: APPLICATION TO THE UINTA MOUNTAINS RANGE

Paul Cavalier[1,2], Alireza Baghai-Wadji[1], Yohann Poprawski[3], Michael Inggs[1]

[1] Department of Electrical Engineering, University of Cape Town, Private Bag X3, Rondebosch 7701, South Africa, email: paul.cavalier@live.fr

[2] Department of Archaeology, University of Cape Town, Private Bag X3, Rondebosch 7701, South Africa

[3] Group of Dynamics of the Lithosphere, Institute of Earth Sciences Jaume Almera, ICTJA-CSIC, Barcelona, 08028, Spain

Accepted date. Received date; in original form date

Abbreviated title: Wavelet Empirical Law

ABSTRACT

Wavelet methods have been used in potential fields study to estimate source properties such as depth or structural index, through the analysis of Wavelet Transform Modulus Maxima Lines (WTMML) intersections and slopes at high scales. Little has been done on the study of maximum points of the wavelet diagram, that we call here Maximum Wavelet Coefficient Scales (MWCS). Previous works have shown interesting correlations between MWCS and source depths, depending on the wavelet used in regards to the source nature and the data derivative order. In this paper, we introduce an empirical law involving spectral parameters that have not been studied so far, which allows analytical calculation of the MWCS, knowing the source characteristics and using certain wavelets. In return, the study of MWCS allows recovering source characteristics from the use of a single wavelet, without prior knowledge on the source.

We demonstrate through synthetic models that the new capability of predicting the source type and depth according to the wavelet coefficient behaviour allows new ways of potential fields' sources characterisation and identification. We show an application of the formula on a real case example in the Uinta Mountains (Utah, USA).

Key words: Wavelet transform, Gravity, Magnetics, Potential Fields, Inverse theory

INTRODUCTION

Data interpretation constitutes an active topic of research in Geophysical exploration, notably for Potential fields (gravity, magnetics, electric self-potentials…), the aim being to recover the maximum of information on causative sources from data measured on the surface, ideally without *a-priori* information. Popular semi-automated techniques such as Euler deconvolution (Reid et al., 1990; Thompson D.T., 1982) allow a quick estimation of source depth, provided the structural index (SI) of the causative body is given. A similar approach is to calculate the Analytic Signal (Nabighian, 1972) and combine it with Euler deconvolution to resolve both location and SI of the source (Keating and Pilkington, 2004). Other analytic methods analyse the signal shape using s-curves (Essa, 2007), ratios of gradients (Cooper, 2012), or local wavenumbers (Salem et al., 2005). Least-squares minimization techniques (Abdelrahman and Essa, 2015; Gupta, 1983;

Lines and Treitel, 1984) are also common to estimate source parameters in comparison to models. A different approach consists in transforming the field using field continuation operators and analysing its transformed diagram. The Continuous Wavelet Transform (CWT) (Fedi et al., 2010; Hornby et al., 1999; Moreau et al., 1999, 1997; Ouadfeul and Aliouane, 2012; Sailhac et al., 2009), or variants such as the Depth-from-Extreme-Points method (Cella et al., 2009; Fedi, 2007)., are good examples of such methodology, and have proved useful with the capacity of recovering source depth and type from the interpretation of the transform diagram, without *a-priori* information.

The method we propose in this paper is in line with these transformation techniques, but differs from all the previous works in the multi-scale spectral identification approach it takes. We will show that signal shapes can be linked to specific spectral parameters that are revealed using wavelet transform. This provides an efficient way of characterising sources, still without *a-priori* information.

The continuous wavelet transform of a signal f with an analysing wavelet Ψ is the convolution of the signal with scaled versions of the wavelet, as follows (Mallat, 1999):

$$W[\Psi, f](t,a) = \int_{-\infty}^{+\infty} dx \frac{1}{\sqrt{a}} \Psi^{*}\left(\frac{t-x}{a}\right) f(x) \qquad (1)$$

in 1D, where $a \in \mathbb{R}^{+}$ is the scale factor, $t \in \mathbb{R}$ the translation factor, x the horizontal coordinate. The asterisk here denotes complex conjugation.

The CWT with γ-order derivative of ψ (γ≥1), applied to the β-order horizontal derivative of f, measured at height z_m, (β≥1) reads:

$$W[\nabla^{\gamma}\Psi, \nabla^{\beta} f_{z_m}](x,a) = \int_{-\infty}^{+\infty} dx \frac{1}{\sqrt{a}} \nabla^{\gamma}\Psi^{*}\left(\frac{t-x}{a}\right) \nabla^{\beta} f_{z_m}(x) \qquad (2)$$

In this paper we introduce a method focusing on the analysis of CWT maximum coefficients (the Maximum Wavelet Coefficient Scale - MWCS), as a direct indicator of source depth and type. Cooper has revealed correspondence of MWCS with source's centre of homogeneity depth (abridged 'source depth' from thereon) when the analysing wavelet is directly inspired from the analysed source function (spherical source, cylindrical source, or also source analytic signal, etc.) (Cooper, 2006). We shall provide an explicit relationship between the MWCS and source depth, including cases when the wavelet and source function are not the same.

The knowledge of such relationship allows directly identifying different source types and depths using a single wavelet. We apply the formula to a real case example over the Uinta Mountains (Utah, USA).

MWCS ANALYSIS

For simplicity we will base our investigation on 3 cases of canonical gravity sources expressions in 1D, the semi-infinite vertical cylinder (VC), the infinite horizontal cylinder (HC) and the sphere (SPH) (Abdelrahman, 1989; Essa, 2007).

The corresponding canonical functions normalized by gravity pre-factors are:

$$f^{VC}(x,z) = \frac{1}{\sqrt{z^2 + x^2}} \qquad (3)$$

$$f^{HC}(x,z) = \frac{z}{z^2 + x^2} \qquad (4)$$

$$f^{SPH}(x,z) = \frac{z}{\left(z^2 + x^2\right)^{3/2}} \qquad (5)$$

Here x denotes the horizontal coordinate, z the vertical coordinate. The following scaling functions can be deduced from eq. (3)-(4)-(5):

$$\psi_{VC}(x) = f^{VC}(x,1) = \frac{1}{\sqrt{1+x^2}} \qquad (6)$$

$$\psi_{HC}(x) = f^{HC}(x,1) = \frac{1}{1+x^2} \qquad (7)$$

$$\psi_{SPH}(x) = f^{SPH}(x,1) = \frac{1}{\left(1+x^2\right)^{3/2}} \qquad (8)$$

The same expressions can be found for magnetic analytic signals, corresponding to different source geometrical features (Cooper, 2006). These scaling functions are then differentiated to obtain the wavelet families $\psi_{VC}^{(\gamma)}$, $\psi_{HC}^{(\gamma)}$ and $\psi_{SPH}^{(\gamma)}$. We recall here that for CWT analysis, the wavelets do not necessarily need to comply with all the conditions usually specified in Discrete Wavelet Transforms (Hornby et al., 1999), concerning orthogonality or compactness for instance.

We then perform the CWT using the different wavelets on each source, with different derivation orders ($\gamma \geq 1$ the derivative order for the wavelets, $\beta \geq 1$ the horizontal derivatives order for the sources). For each case, we take the MWCS/Source-depth ratio (M-Z ratio) and compile it in Table 1. We only take derivative orders satisfying the constraint $|\gamma - \beta| = 2n$ ($n \in \mathbb{N}$), to preserve the same parity between analysing wavelet and analysed function. This parity condition between both functions allows the MWCS to be located straight above the source.

*Table 1. M-Z ratio measurements combining all wavelets and functions at different orders of derivation. Each sub-table shows the result using 1 wavelet family (PSI-VC -vertical cylinder, PSI-HC – horizontal cylinder, PSI-SPH – sphere) with the γ-derivatives, on the functions f^{VC}, f^{HC}, f^{SPH} and their β-derivatives. We have taken the cases where Z_m=1 so that MWCS=M-Z ratio. The data is sampled with xstep=0.01. We show the value measured by the CWT (MES=MWCS*0.01), the value given by the empirical law (equation (20)), and the relative error. We limit γ , β = [1, 2, 3, 4] for clarity.*

	PSI-VC	γ = 1			γ = 2			γ = 3			γ = 4		
f-deriv		MES	LAW	*%*	MES	LAW	*%*	MES	LAW	*%*	MES	LAW	*%*
β = 1	fVC	1,03	1	*3*				2,82	3	*-6*			
	fHC	0,74	0,667	*11*				2,05	2	*2*			
	fSPH	0,59	0,5	*18*				1,67	1,5	*11*			
β = 2	fVC				1,02	1	*2*				2,04	2	*2*

	fHC				0,82	0,8	*2*				1,6	1,6	*0*
	fSPH				0,71	0,67	*6*				1,41	1,33	*6*
β = 3	fVC	0,35	0,33	*6*				1,03	1	*3*			
	fHC	0,31	0,28	*11*				0,91	0,86	*6*			
	fSPH	0,28	0,25	*12*				0,77	0,75	*3*			
β = 4	fVC				0,51	0,5	*2*				1,02	1	*2*
	fHC				0,43	0,44	*-2*				0,9	0,89	*1*
	fSPH				0,43	0,4	*7*				0,79	0,8	*-1*

	PSI-HC	γ = 1			γ = 2			γ = 3			γ = 4		
f-deriv		MES	LAW	*%*	MES	LAW	*%*	MES	LAW	*%*	MES	LAW	*%*
β = 1	fVC	1,42	1,5	*-5*				3,32	3,5	*-5*			
	fHC	1,03	1	*3*				2,28	2,33	*-2*			
	fSPH	0,82	0,75	*9*				1,88	1,75	*7*			
β = 2	fVC				1,23	1,25	*-2*				2,26	2,25	*0*
	fHC				1,02	1	*2*				1,8	1,8	*0*
	fSPH				0,85	0,83	*2*				1,53	1,5	*2*
β = 3	fVC	0,49	0,5	*-2*				1,17	1,166	*0*			
	fHC	0,41	0,43	*-5*				1,04	1	*4*			
	fSPH	0,38	0,375	*1*				0,89	0,875	*2*			
β = 4	fVC				0,62	0,625	*-1*				1,15	1,12	*3*
	fHC				0,51	0,55	*-7*				1,03	1	*3*
	fSPH				0,51	0,5	*2*				0,92	0,9	*2*

	PSI-SPH	γ = 1			γ = 2			γ = 3			γ = 4		
f-deriv		MES	LAW	*%*	MES	LAW	*%*	MES	LAW	*%*	MES	LAW	*%*
β = 1	fVC	1,71	2	*-15*				3,73	4	*-7*			

	fHC	1,27	1,33	*-5*				2,57	2,67	*-4*			
	fSPH	1,03	1	*3*				2,06	2	*3*			
β = 2	fVC				1,41	1,5	*-6*				2,43	2,5	*-3*
	fHC				1,19	1,2	*-1*				2,04	2	*2*
	fSPH				1,02	1	*2*				1,7	1,67	*2*
β = 3	fVC	0,61	0,67	*-9*				1,28	1,33	*-4*			
	fHC	0,53	0,57	*-7*				1,13	1,14	*-1*			
	fSPH	0,52	0,5	*4*				1,04	1	*4*			
β = 4	fVC				0,73	0,75	*-3*				1,23	1,25	*-2*
	fHC				0,65	0,67	*-3*				1,02	1,1	*-7*
	fSPH				0,6	0,6	*0*				1,02	1	*2*

In order to find the correct relationship governing the M-Z ratio, let us consider the Fourier transforms of the source functions. These can be written as modified Bessel functions of second kind (Bessel-K_ν functions) (Mathematica, 2016) :

$$F_x^{VC}\left[\frac{1}{\sqrt{z^2+x^2}}\right](\omega)=\sqrt{\frac{2}{\pi}}K_0(z\omega) \qquad (9)$$

$$F_x^{HC}\left[\frac{z}{z^2+x^2}\right](\omega)=\sqrt{\frac{\pi}{2}}e^{-z\omega}=\sqrt{z\omega}K_{1/2}(z\omega) \qquad (10)$$

$$F_x^{SPH}\left[\frac{z}{\left(z^2+x^2\right)^{3/2}}\right](\omega)=\sqrt{\frac{2}{\pi}}\omega K_1(z\omega) \qquad (11)$$

We consider the Bessel function order ν as the important parameter. We note $\nu_{VC}=0$, $\nu_{HC}=1/2$ $\nu_{SPH}=1$. The empirical law we derive is:

$$a_{\max}=\frac{\gamma+\nu_\Psi}{\beta+\nu_F}z_m \qquad (12)$$

Here, a_{max} is the MWCS, z_m the height of measurement (opposite of the source depth), ν_Ψ the order of the Bessel-K function corresponding to the Fourier transform of the scaling function used, ν_F the order of the Bessel-K function corresponding to the Fourier transform of the source function (not derived). Hence $\nu_{\Psi,F} = \nu_{VC}$ for the $\psi_{VC}^{(\gamma)}$ family and f^{VC} function, $\nu_{\Psi,F} = \nu_{HC}$ for $\psi_{HC}^{(\gamma)}$ and f^{HC}, and $\nu_{\Psi,F} = \nu_{SPH}$ for $\psi_{SPH}^{(\gamma)}$ and f^{SPH}.

As Table 1 shows, this empirical law yields M-Z ratios very close to the ones measured for all these source types, wavelet types, and for all γ and β derivative orders for sources and wavelets, with relative errors below 5% in about 70% of the cases. The error may originate from both numerical sampling processes in the computer program and from possible inaccuracies of the empirical law.

To test the noise impact on the results, we have added a random Gaussian noise with a standard deviation of 5% and 15% of the signal maximum amplitude before realizing the CWT. We show in Table 2 a summary of the results for the $\psi_{HC}^{(\gamma)}$ wavelet family, on all source functions. We can see that the average of the error absolute values is still very low, at 4% and 7% respectively for 5% noise and 15% noise, whereas that average was about 3% without noise. Similar results can be obtained for the other wavelet families.

Table 2. M-Z ratio measurements for the PSI-HC – horizontal cylinder wavelet family, and functions f^{VC}, f^{HC}, f^{SPH} at β orders of derivation, with noise applied on the data before CWT. The first sub-table shows the values for 5% Gaussian noise, the second at 15% noise.

5% noise	PSI-HC	γ = 1			γ = 2			γ = 3			γ = 4		
f-deriv		MES	LAW	%	MES	LAW	%	MES	LAW	%	MES	LAW	%
β = 1	fVC	1,38	1,5	*-8*				3,28	3,5	*-6*			
	fHC	1,02	1	*2*				2,29	2,33	*-2*			
	fSPH	0,77	0,75	*3*				1,89	1,75	*8*			
β = 2	fVC				1,2	1,25	*-4*				2,36	2,25	*5*
	fHC				1,03	1	*3*				1,82	1,8	*1*
	fSPH				0,88	0,83	*6*				1,54	1,5	*3*
β = 3	fVC	0,51	0,5	*2*				1,09	1,166	*-7*			
	fHC	0,46	0,43	*7*				1,04	1	*4*			
	fSPH	0,39	0,375	*4*				0,94	0,875	*7*			
β = 4	fVC				0,62	0,625	*-1*				1,13	1,12	*1*
	fHC				0,52	0,55	*-5*				1,03	1	*3*
	fSPH				0,52	0,5	*4*				0,93	0,9	*3*

15% noise	PSI-HC	γ = 1			γ = 2			γ = 3			γ = 4		
f-deriv		MES	LAW	%	MES	LAW	%	MES	LAW	%	MES	LAW	%
β = 1	fVC	1,34	1,5	*-11*				3,27	3,5	*-7*			
	fHC	0,96	1	*-4*				2,31	2,33	*-1*			
	fSPH	0,88	0,75	*17*				1,98	1,75	*13*			
β = 2	fVC				1,38	1,25	*10*				2,19	2,25	*-3*
	fHC				0,89	1	*-11*				1,72	1,8	*-4*
	fSPH				0,9	0,83	*8*				1,67	1,5	*11*
β = 3	fVC	0,53	0,5	*6*				1,34	1,166	*15*			
	fHC	0,45	0,43	*5*				1,08	1	*8*			
	fSPH	0,41	0,375	*9*				0,95	0,875	*9*			
β = 4	fVC				0,62	0,625	*-1*				1,06	1,12	*-5*
	fHC				0,58	0,55	*5*				0,99	1	*-1*
	fSPH				0,52	0,5	*4*				0,97	0,9	*8*

Such a formula allows source characterisation from the analysis of MWCS using a single wavelet, with the following method:

Perform the CWT on a β_1-derivative of the data with a wavelet of same derivative order ($\gamma=\beta_1$), and CWT on a β_2-derivative of the data ($\beta_2 = \beta_1 \pm 2n$, $n \in \mathbb{N}$, and $\beta_1,\beta_2>0$).

Measure the MWCS for each case, yielding a_{max1} and a_{max2}. According to eq. (12), we can write:

$$\frac{a_{\max 2}}{a_{\max 1}} = \frac{\beta_1 + \nu_F}{\beta_2 + \nu_F} \qquad (13)$$

Then recover ν_F through:

$$\nu_F = \frac{-(\beta_2 - \beta_1)}{\frac{a_{\max 2}}{a_{\max 1}} - 1} - \beta_2 \qquad (14)$$

ν_F allows us to identify the original Bessel-K function that is characteristic of the source's Fourier transform, and consequently we can resolve the source type.

The knowledge of ν_F, along with already knowing the other parameters (a_{max}, γ, β, ν_Ψ), allows recovering z_m via eq. (12).

We illustrate this method on 2 synthetic examples using Matlab: in Fig. 1 with a vertical cylinder with the top at depth -1, hence height of measurement z_m=1, and in Fig. 2 with a sphere with center at z_m=3. The data is sampled at x_{step}=0.01. That sampling impacts the scaling and thus the results for z_m need to be multiplied by 0.01 to reach the real values. We purposefully use a wavelet from a different family, the $\psi^{(\gamma)}{}_{HC}$ family (horizontal cylinder - ν_Ψ = 0.5), with γ=2.

For the vertical cylinder, application of eq.(8) yields ν_F=0.10, and the subsequent application of eq.(12) respectively with β_1=2 and β_2=4 (with a_{max}=123 and a_{max}=63) yields z_m=1.034 and 1.033.

For the sphere, application of eq.(12) yields ν_F=1.00, and the subsequent application of eq.(14), respectively, with β_1=2 and β_2=4 (with a_{max}=255 and a_{max}=153) yields z_m=3.06 in both cases.

These results are in very good agreement with the expected values: 1 and 3 for z_m, 0 and 1 for ν_F, respectively, for the vertical cylinder and sphere examples, despite using a wavelet from a different family, thus validating the consistency of the method. Other wavelet/data combinations lead to results with similarly good accuracy, provided the M-Z ratio initial relative errors as shown in Table 1 are low. This adds credit to the fact that the MWCS can be used in an advantageous way for inversion methods as a physically-based weighting procedure (Cavalier, 2015a, 2015b; Roshandel Kahoo et al., 2015).

A common method used in the community is the Euler deconvolution (Reid et al., 1990; Thompson D.T., 1982). We show in Fig. 3 an implementation of Euler deconvolution with the solutions displayed on the CWT diagram, for two canonical sources (Vertical and Horizontal cylinders), buried at z_m=1. We perform the CWT analysis and Euler deconvolution on the first horizontal derivatives of the signals. All CWT diagrams in this paper show the coefficients' absolute values, so positive or negative anomalies are highlighted the same way.

The Euler solutions vary according to the structural index (SI) and the window of analysis chosen, which we chose to be 51 according to recommendations in (Reid et al., 2014). In this implementation, both Vertical and Horizontal cylinders having a SI=1, the same Euler deconvolution can be run, giving slightly different depths in each case: 0.82 for vertical cylinder top, 0.7 for horizontal cylinder core). We implement the CWT, using wavelets identical to the source signals (psiVC1 on dx1_VC, psiHC1 on dx1_HC), and then exchanging them (psiVC1 on dx1_HC, and psiHC1 on dx1_VC).

On one hand, we observe that with the above chosen parameters the Euler solutions always underestimate the true depth (z_m=1 hence scale value of 100 because of the data sampling rate), while the MWCS matches the right depth when the wavelet used corresponds to the source function. On the other hand, the MWCS deviation when wavelet and source function differ can be predicted using the empirical law we present (Eq.12). Such an analytic correction is not possible with the Euler deconvolution method, and is in return an asset of the approach we propose.

With the ability to predict the MWCS behaviour, the use of CWT becomes more flexible as different wavelet families can be chosen. In the case where a first depth approximation is required, for instance as a weighting matrix for inversion, we suggest performing the CWT using the first derivative of the Horizontal Cylinder family (psiHC1), on the first horizontal derivative of the data (dx1). The Horizontal Cylinder family providing MWCS at intermediate values compared to the Vertical Cylinder or Spherical source families, and the first derivative of the data having less noise than higher order derivatives, the overall result would minimize the depth error. A more detailed study as we present in this paper allows refining the model if necessary.

Finally, we observe that a source gives rise to a 'cloud' of stronger coefficients on the CWT diagram, which can be problematic if sources are not well isolated, as wavelet coefficients can coalesce together. Recent developments in wavelet transforms, namely the synchro-squeezed transform (Daubechies et al., 2011), reduce the smearing of wavelet coefficient profiles in the transform diagram by re-assigning the scales. This in turn can reduce the sensitivity of the method to interferences caused by nearby sources. We will not address this topic in this presentation as our principal focus is on the general CWT and the empirical law derived in its context. We should keep in mind nonetheless that additional possibilities are offered by wavelet methods, and can optimize the process further.

COMPARISON WITH PREVIOUS WAVELET METHODS

As mentioned previously in (Cooper, 2006), performing the CWT with wavelets directly inspired from the analysed function yields good correspondence between MWCS and source depths. Indeed we observe in Table 1 that the M-Z ratios when γ=β and $\psi(x) = f(x,1)$ remain stationary and close to 1 within 5% relative error. Otherwise, the MWCS deviates from the source depth, which deviation can now be quantified using eq.(12).

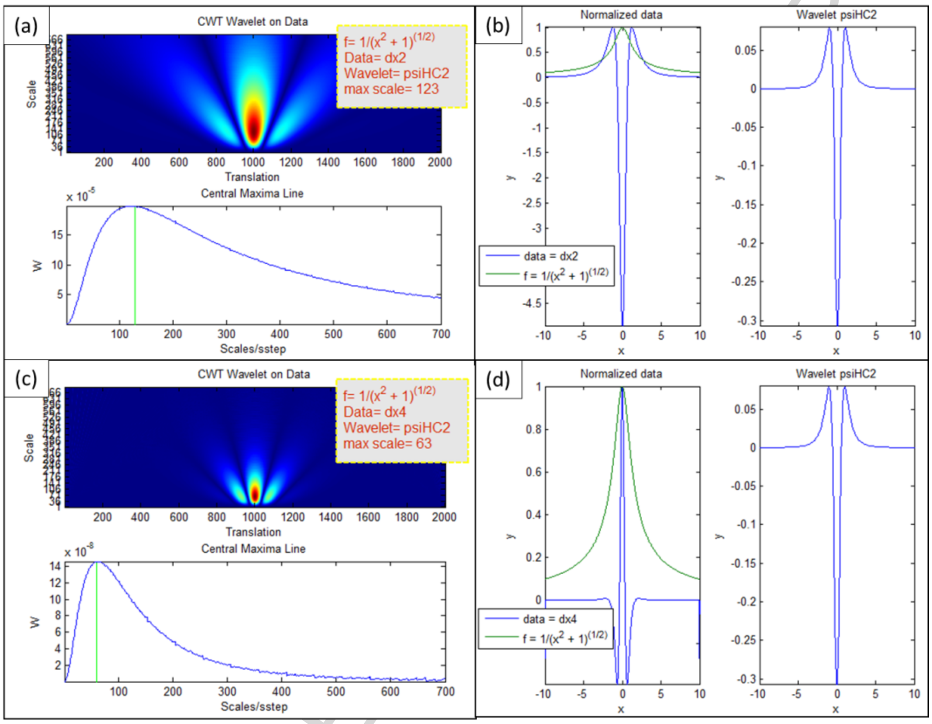

Fig.1 Analysis of a vertical cylinder buried at depth z=1, with a wavelet from the horizontal cylinder family. (a) CWT absolute values diagram with wavelet named 'psiHC2' (2^{nd} derivative of ψ_{HC}), on 'data' being the 4^{th} horizontal derivative of f^{VC}, with the central maxima line profile indicating the maximum scale. Red color indicates strong coefficients, blue color weak coefficients. (b) profiles of the corresponding data and wavelet. (c) CWT absolute values diagram with wavelet named 'psiHC2' (2^{nd} derivative of ψ_{HC}), on 'data' being the 2^{nd} horizontal derivative of f^{VC}, with the central maxima line profile indicating the maximum scale. Red color indicates strong coefficients, blue color weak coefficients. (d) profiles of the corresponding data and wavelet.

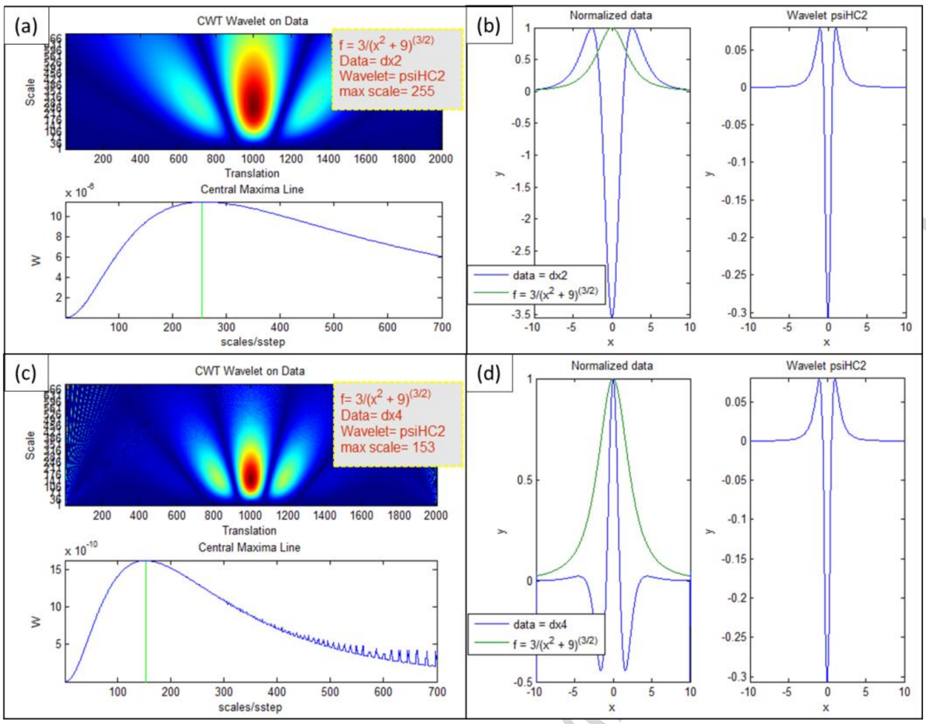

Fig.2 Analysis of a sphere buried at depth z=3, with a wavelet from the horizontal cylinder family. (a) CWT absolute values diagram with wavelet named 'psiHC2' (2nd derivative of ψ_{HC}), on 'data' being the 2nd horizontal derivative of f^{SPH}, with the central maxima line profile indicating the maximum scale. (b) profiles of the corresponding data and wavelet. (c) CWT absolute values diagram with wavelet named 'psiHC2' (2nd derivative of ψ_{HC}), on 'data' being the 4th horizontal derivative of f^{SPH}, with the central maxima line profile indicating the maximum scale. (d) profiles of the corresponding data and wavelet.

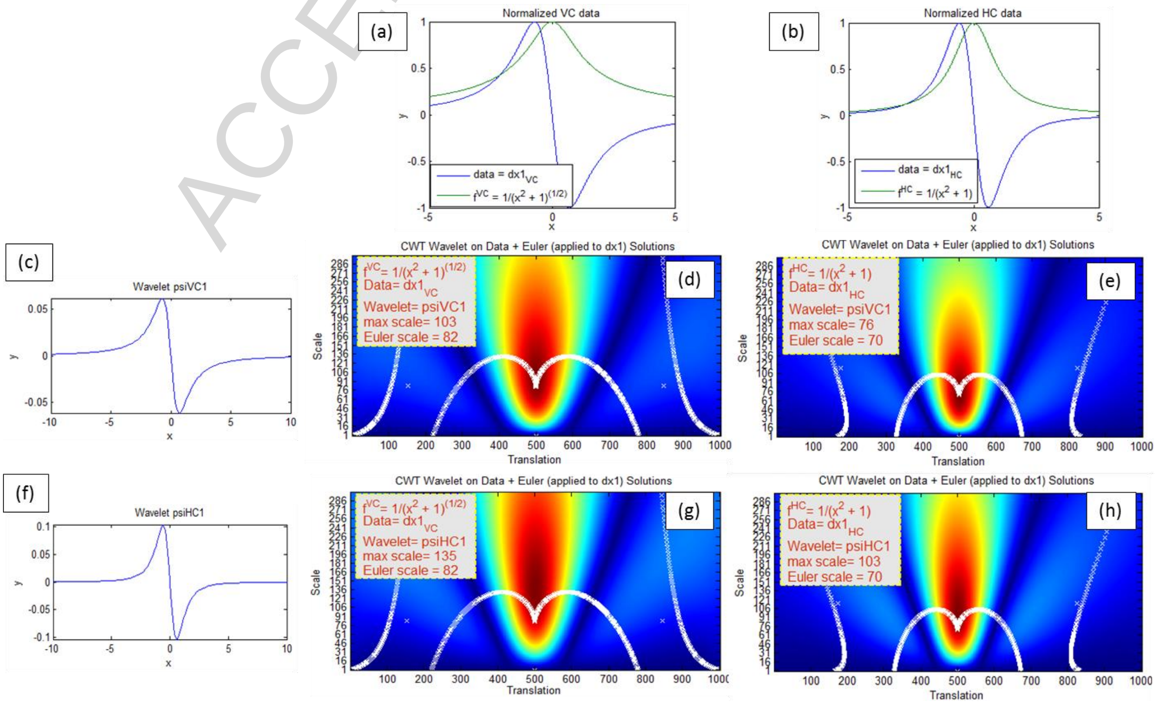

Fig.3 Comparison of wavelet diagrams for buried vertical cylinder (VC) and horizontal cylinder (HC) cases, with Euler solutions (white crosses) calculated on first horizontal derivative of data 'dx1_VC' and 'dx1_HC', for SI=1 and window=51.
Fig. (a) and (b): normalized data for Vertical cylinder and Horizontal cylinder cases, respectively, buried at z=1. The first horizontal

derivative 'dx1' is shown by the blue line. Fig. (c) and (f): analyzing wavelets used, as first derivatives of the Vertical cylinder ('psiVC1') and Horizontal cylinder ('psiHC1') families, respectively. Fig. (d)-(e)-(g)-(h): CWT absolute values diagrams using corresponding dx1 and wavelets of the table. The maximum wavelet coefficient scale is shown, as well as the matching Euler scale at the center of the diagram.

Furthermore, we can compare the empirical law to other theories developed previously, following the reasoning developed in (Moreau et al., 1997). Reverting to eq. (2), we calculate the wavelet transform in Fourier domain, thus the convolution becoming a product of Fourier transforms:

$$\begin{aligned}
&\hat{W}[\nabla^{\gamma}\Psi,\nabla^{\beta} f_{z_m}](k,a)\\
&=\sqrt{a}\,\hat{\Psi}^{(\gamma)}(ak)\hat{F}_{z_m}^{(\beta)}(k)\\
&=\sqrt{a}\,(-iak)^{\gamma}\,\hat{\Psi}(ak)(-ik)^{\beta}\,\hat{F}_{z_m}(k)\\
&=a^{\gamma+\frac{1}{2}}(-ik)^{\gamma+\beta}\,\hat{\Psi}(ak)\hat{F}_{z_m}(k)
\end{aligned} \quad (15)$$

In Potential Field analysis, the choice of the wavelet can be guided by the mathematical properties of potential fields: they are harmonic functions that satisfy Laplace's equation (Blakely, 1996, page 8). They can be chosen to preserve the property of field continuation, so that the result of the convolution is equivalent to the field prolonged to a certain scale. Functions with such property belong to the Poisson Kernel, and have the following form (for $h \in \mathbb{R}^n$ being the horizontal coordinates, $a \in \mathbb{R}$ being the vertical coordinate) (Sailhac et al., 2009):

$$P_a(h)=\frac{1}{n\pi}\frac{a}{\left(|h|^2+a^2\right)^{\frac{n+1}{2}}} \quad (16)$$

After equation (2), the CWT with wavelets of the Poisson kernel writes:

$$W[\nabla^{\gamma}P_1,\nabla^{\beta} f_{z_m}](x,a)=\int_{-\infty}^{+\infty} dx\,\frac{1}{\sqrt{a}}\nabla^{\gamma}P_1^{*}\left(\frac{t-x}{a}\right)\nabla^{\beta} f_{z_m}(x) \quad (17)$$

Continuing from eq. (15), as we have functions for which Fourier transforms are decreasing exponentials, we can write:

$$\begin{aligned}
&\hat{W}[\nabla^{\gamma}P_1,\nabla^{\beta} f_{z_m}](k,a)\\
&=a^{\gamma+\frac{1}{2}}(-ik)^{\gamma+\beta}\,\hat{P}_1(ak)\hat{F}_{z_m}(k)\\
&=a^{\gamma+\frac{1}{2}}(-ik)^{\gamma+\beta}\,e^{-a|k|}e^{-z_m|k|}\\
&=a^{\gamma+\frac{1}{2}}(-ik)^{\gamma+\beta}\,\hat{F}_{a+z_m}(k)\\
&=a^{\gamma+\frac{1}{2}}\hat{F}_{a+z_m}^{(\gamma+\beta)}(k)
\end{aligned} \quad (18)$$

Hence, the inverse Fourier transform yields:

$$W[\nabla^{\gamma}P_1,\nabla^{\beta} f_{z_m}](x,a)=a^{\gamma+\frac{1}{2}}\nabla^{\gamma+\beta} f_{a+z_m}(x) \quad (19)$$

This result means that the CWT diagram using a wavelet from the Poisson Kernel, applied to a source field of same form, is equivalent to an upward continued field times a scale factor (Archibald et al., 1999).

If we consider f as a field created by a homogeneous source, f is homogeneous of order α_f and we can rewrite the CWT result:

$$W[\nabla^{\gamma} P_1, \nabla^{\beta} f_{z_m}](x,a) = a^{\gamma+\frac{1}{2}} \left(a+z_m\right)^{\alpha_f-\beta-\gamma} \nabla^{\gamma+\beta} f_1\left(\frac{x}{a+z_m}\right) \qquad (20)$$

This formula is the starting formula for Moreau et al.'s interpretation of the CWT diagram, using maxima lines intersection below the CWT plane to recover source depth, and slopes of the maxima lines at high scales to recover source homogeneity order and its structural index.

We adopt a different strategy, which is to study the maximum coefficients occurring in the diagram, in order to recover the sources' depths. With the parity condition respected as mentioned earlier, the horizontal locations of these sources are naturally determined by the locations of the anomalies in the signal. From eq. (20), we place ourselves above the source (x=0), so the source depth is controlled by the function:

$$g(a) = a^{\gamma+\frac{1}{2}} \left(a+z_m\right)^{\alpha_f-\beta-\gamma} \qquad (21)$$

The condition $\frac{\partial g}{\partial a}(a) = 0$ then leads to:

$$a_{\max} = \frac{\gamma+\frac{1}{2}}{\beta-\alpha_f-\frac{1}{2}} z_m \qquad (22)$$

This equation linking the maximum scale to the source depth highly resembles the empirical law we give. In fact, it describes correctly the M-Z ratio in the horizontal cylinder case where α_f = -1, and with ψ_{HC} as analysing wavelet. In that case, we have $\nu_\Psi = \nu_F = 0.5$ and equations (12) and (22) are both equivalent to:

$$a_{\max} = \frac{\gamma+\frac{1}{2}}{\beta+\frac{1}{2}} z_m \qquad (23)$$

Equation (22) fails to describe the other cases, when the same ψ_{HC} analysing wavelet is applied to a spherical source (α_f = -2) or a vertical cylinder (α_f = -1).

We suggest that this discrepancy originates from the transitions in eq. (18). Indeed the product of Fourier transforms will yield a simple exponential containing the sum of arguments only if the Fourier transforms are simple exponentials individually. As it is shown in eqs. (9) and (11), that is not the case for sources other than the horizontal cylinder: the vertical cylinder or the sphere have characteristic functions whose Fourier transforms can be written as Bessel-K functions, which cannot be simplified as decreasing exponentials (unlike the horizontal cylinder case).

This also implies that 1D upward continuation techniques, based on building the product of the Fourier transform of the data with a decreasing exponential, are strictly speaking inaccurate in general, except for data originating from horizontal cylinders. This stems from the fact that the exponential function is the eigenfunction of the second-order differential operator $\frac{\partial^2}{\partial z^2}$ in a Cartesian coordinate system, where the eigenfunctions are separable, factorizable functions (involving exponential functions), but not in general curvilinear coordinate systems. Consequently, the ideas underlying exponential continuation techniques can be adapted in curvilinear coordinate systems only along specific coordinates and subject to more stringent conditions which are outside the scope of this disposition. In the present case the horizontal cylinder can be described accurately by eq. (4) in all planes above the cylinder; eqs. (3) and (5) describe, respectively, the vertical cylinder and the sphere only along a profile situated directly above the source.

REAL CASE EXAMPLE: APPLICATION TO THE UINTA MOUNTAINS RANGE

4.1 GEOLOGICAL SETTING

The Uinta Mountains, East of Salt Lake City (Utah, USA) belongs to the Rocky Mountains and are described as an E-W striking anticline-like structure, bounded by thrusts dipping north in the southern flank and south in the northern flank, forming a pop-up structure (Gries, 1983; Stone, 1993). This E-W striking pop-up is oblique to the main N-S striking Sevier-Laramide thrust-belt (Paulsen and Marshak, 1999). The core of the pop-up is composed of Paleoproterozoic metasedimentary rocks (Hansen, 1965) and of up to 7 km thick Neoproterozoic sandstones and mudstones (Kingsbury-Stewart et al., 2013). The flanks of the pop-up are made of Palaeozoic (mainly Cambrian and Carboniferous) and of Mesozoic rocks (Hansen, 1965). The younger deposits found in the flanks are Paleocene to Quaternary in age. Tertiary sedimentary rocks are associated with Late Miocene to Pliocene basalt flows (e.g., (Hintze et al., 2000)).

The geological history of the Uinta Mountains results from a complex succession of orogenic phases from Precambrian to Cenozoic (Bird, 1998). The first event corresponds to the formation of the Cheyenne Suture formed at 1.8 G.a (Crosswhite and Humphreys, 2003), inducing metamorphism of the Paleoproterozoic metasedimentary rocks. From Aptian to Early Eocene, shortening is assumed to occur forming the Sevier orogenic belt, which is an eastward-propagating thrust-belt, located west of the Uinta Mountains (Decelles et al., 1995; Heller and Paola, 1989). From Campanian to Late Eocene, the Laramide orogeny affected the area of the Uinta Mountains (Dickinson et al., 1988; Paulsen and Marshak, 1999). The Sevier-Laramide thrust-belt formed in response to the subduction of the Farallon oceanic plate beneath the North American continental plate from Jurassic to Paleogene (Burchfiel and Lipman, 1992; DeCelles, 2004; English et al., 2003; Weil and Yonkee, 2012). During Late Oligocene, extension affected the area and caused the opening of the Rio-Grande rift, in Colorado and New Mexico (Constenius, 1996). Extension was coeval with uplift of the Colorado Plateau (McMillan et al., 2006) and volcanism, which are interpreted to result from a thermic event, warming the lithosphere (Roy et al., 2009).

4.2 MWCS STUDY OF GRAVITY DATA

We use the gravity survey data over Utah (USA), compiled by the National Oceanic and Atmospheric Administration and available on their online database (Cook et al., 1990). We focus on the Uinta Mountains area, which is well isolated and visible on the gravity survey, as shown in Fig. 4. We choose 3 sections across the mountain range as shown in Fig. 5.

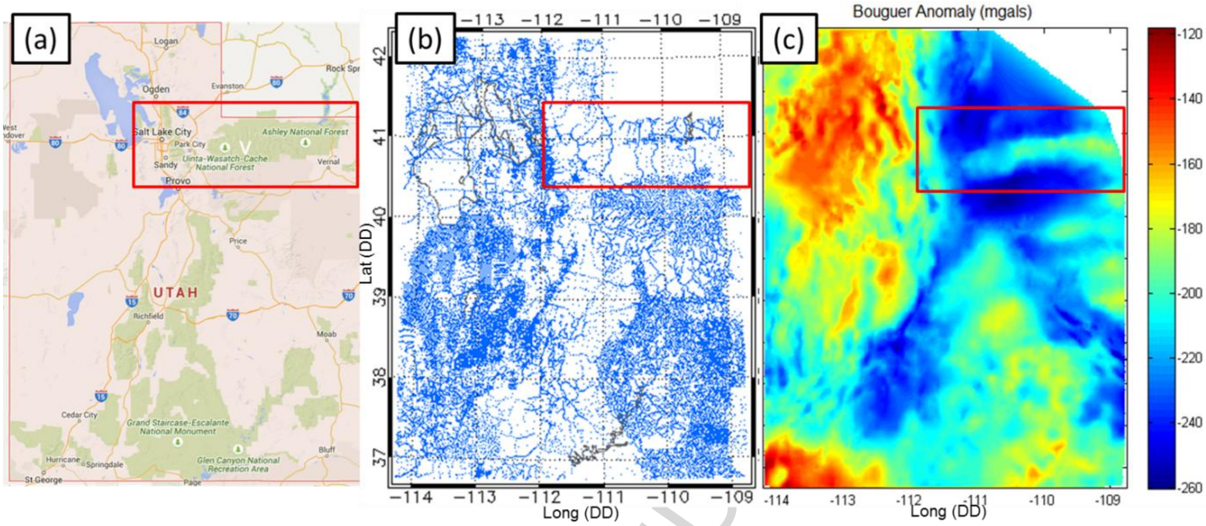

Fig.4 (a) Geographical map of Utah, USA. The red insert encloses the Uinta Mountains. (b) Compilation of gravity surveys in Utah (Cook et al., 1990). Axis indicate latitude and longitude coordinates (DD), blue dots correspond to the points of survey. (c) Representation of the Bouguer anomaly (mgals) across the state. Grid cell size is 2.89 km.

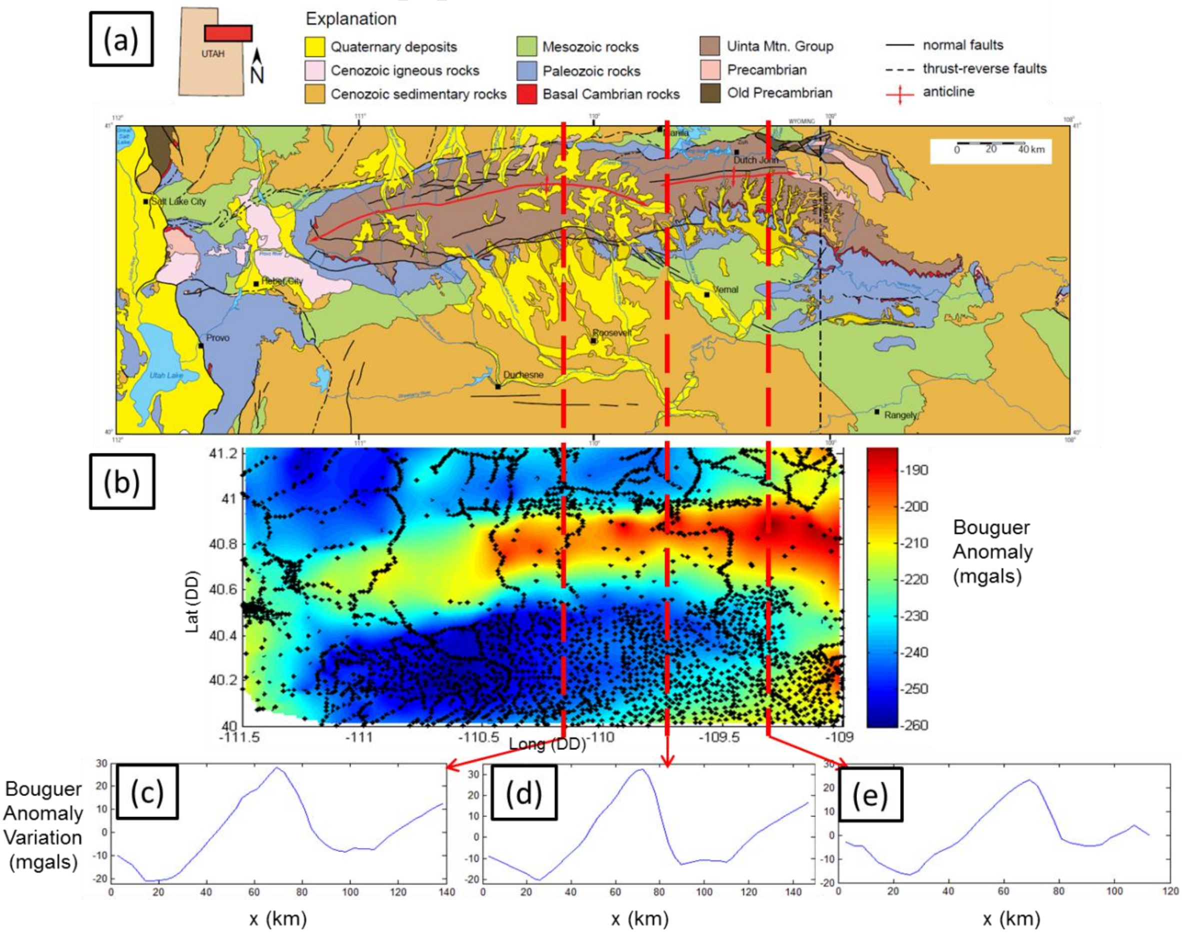

Fig.5 (a) Geologic map of the Uinta Mountains, adapted from (Sprinkel, 2014)*. The red dashes indicate the measurement sections. (b) Bouguer anomaly map (mgals) over the Uinta Mountains, corresponding to upper right corner of Figure 3(b). Axis indicate latitude and longitude coordinates (DD), black dots correspond to the points of survey. (c), (d), (e) are the Bouguer anomaly profiles (mgals) vs. distance for the three sections in red, respectively named "Profile A", "Profile B", "Profile C" subsequently.*

To study the potential of the method irrespective of the wavelet, we use all three families of wavelets $\psi_{VC}^{(\gamma)}$, $\psi_{HC}^{(\gamma)}$ and $\psi_{SPH}^{(\gamma)}$ for a full comparison. We perform the CWT with the first (resp. second) derivative of these wavelets, on the first (resp. second) derivative of the signals, to exhibit the evolution of the MWCS and their ratios. Figs. 6, 7, 8 show the resulting CWT along the profiles. Euler solutions applied to the first horizontal derivative of the data ('dx1') are shown as white crosses on the diagrams, using SI=0 (contact model) and a window of 5. Numerical values of MWCS are summarized in Table 3, and compared to theoretical ratios extracted from Table 1. We observe in particular how the MWCS evolves when γ=β, depending on the chosen wavelet family. A stationary MWCS from an order to another is a good indication that the analysed function corresponds to the wavelet used. The evolution of the MWCS for other wavelets can be compared to the synthetic cases as a confirmation.

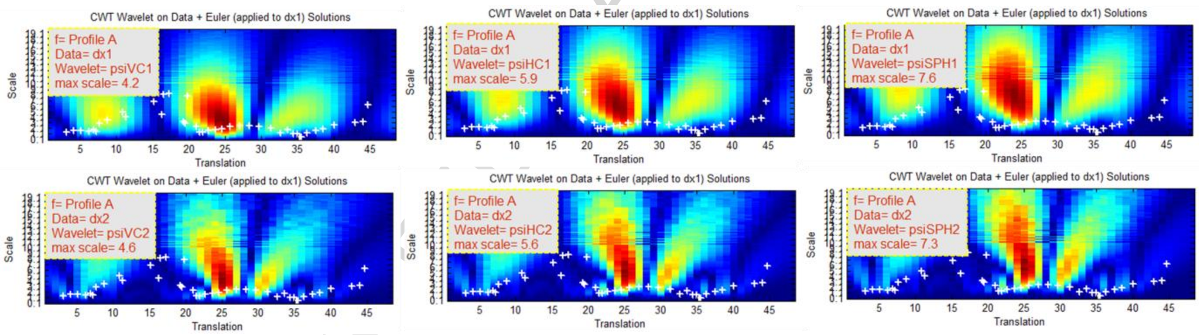

Fig.6 CWT realised on "Profile A" (shown in Fig. 4(c)), on 'dx1'- 1st horizontal derivative of data (β=1), 'dx2'- 2nd horizontal derivative of data (β=2), with all three wavelet families, with same derivative order (γ=1, resp. γ=2). White crosses indicate Euler solutions applied to dx1, with SI=0 and window of 5. 'Translation' indicates the cell number, each cell corresponding to the gridding size of 2.89km.

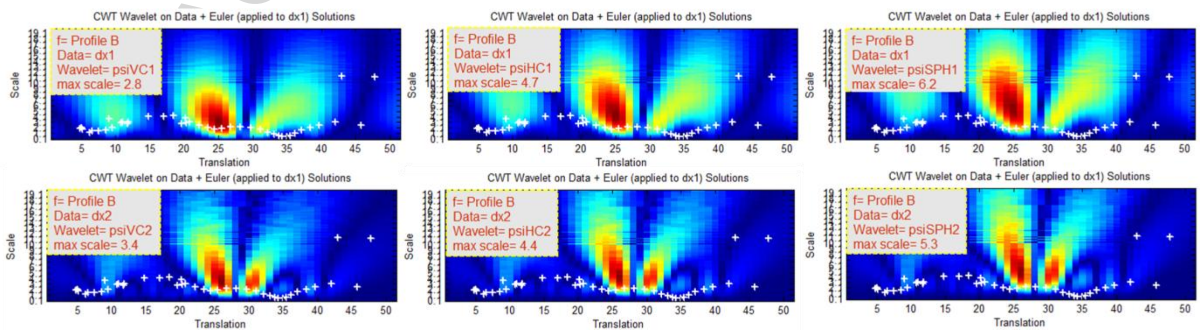

Fig.7 CWT realised on "Profile B" (shown in Fig. 4(d)), on 'dx1'- 1st horizontal derivative of data (β=1), 'dx2'- 2nd horizontal derivative of data (β=2), with all three wavelet families, with same derivative order (γ=1, resp. γ=2). White crosses indicate Euler solutions applied to dx1, with SI=0 and window of 5. 'Translation' indicates the cell number, each cell corresponding to the gridding size of 2.89km.

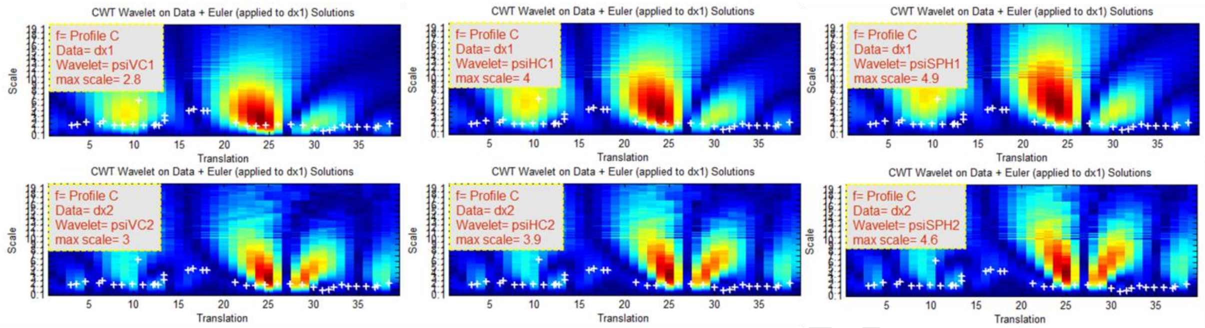

Fig.8 CWT realised on "Profile C" (shown in Fig. 4(e)), on 'dx1'- 1st horizontal derivative of data (β=1), 'dx2'- 2nd horizontal derivative of data (β=2), with all three wavelet families, with same derivative order (γ=1, resp. γ=2). White crosses indicate Euler solutions applied to dx1, with SI=0 and window of 5. 'Translation' indicates the cell number, each cell corresponding to the gridding size of 2.89km.

Table 3. MWCS measured on Profiles A, B and C, using the three wavelet families, with β=γ pairs of values 1 and 2. Values in bold are measured as in Figs. 5-6-7. Values in italic indicate the theoretical values obtained for the HC (Horizontal cylinder) or VC (Vertical cylinder) cases, using the underlined reference value as source depth, multiplied by the theoretical ratios. These theoretical ratios are given in the two sub-tables, as summarized from Table 1, with the CWT realized on the f^{HC} and f^{VC} synthetic cases. The corresponding errors (%) are indicated.

MWCS Measured	Psi-VC	Psi-HC	Psi-SPH
Profile A - DX1 (β=1, γ=1)	3,6	6	7,8
	HC 3,74 / -3,7%	*HC <u>5,6</u> / 7%*	*HC 7,44 / 4,8%*
	VC <u>4</u> / -10%	*VC 6 / 0%*	*VC 8 / -2,5%*
Profile A - DX2 (β=2, γ=2)	4	5,4	7,4
	HC 4,4 / -9%	*HC <u>5,6</u> / -3,5%*	*HC 6,6 / 12%*
	VC <u>4</u> / 0%	*VC 5 / 8%*	*VC 6 / 23%*
Profile B - DX1 (β=1, γ=1)	3,2	4,8	6,2
	HC 3,06 / 4,5%	*HC <u>4,6</u> / 4,3%*	*HC 6,12 / 1,3%*
Profile B - DX2	4	4,4	5,4

(β=2, γ=2)	*HC 3,68 / 8,7%*	*HC 4,6 / -4,3%*	*HC 5,52 / -2%*
Profile C - DX1 (β=1, γ=1)	2,8	4,2	5
	HC 2,66 / 5,2%	*HC 4 / 5%*	*HC 5,32 / -6%*
Profile C - DX2 (β=2, γ=2)	3,4	4	4
	HC 3,2 / 6,2%	*HC 4 / 0%*	*HC 4,8 / -16%*

Theorical ratios - f^{VC}	Psi-VC	Psi-HC	Psi-SPH
DX1 (β=1, γ=1)	1	1,5	2
DX2 (β=2, γ=2)	1	1,25	1,5

Theorical ratios - f^{HC}	Psi-VC	Psi-HC	Psi-SPH
DX1 (β=1, γ=1)	0,667	1	1,33
DX2 (β=2, γ=2)	0,8	1	1,2

We first notice that Euler solutions do not always give clear clusters, due to a low number of data in each dataset, which renders source localisation difficult. This contrasts in turn with the wavelet coefficients which clearly highlight the anomalies in the signal. The horizontal and vertical locations of Euler clusters also generally differ from the MWCS locations, and tend to be located at lower scales (and thus depths).

When analysing the MWCS evolution from a CWT to another, we also observe that the MWCS for profiles B and C correspond well to the f^{HC} (Horizontal Cylinder) case, which correlates with the visual inspection of the map. We further proceed to the depth calculation of the core of that cylinder. To do so, we calculate the gridding distance on the field using the GPS coordinates, yielding a gridding of 2.892 km between data points on the overall 200×200 data matrix. Using the mean MWCS points from the CWT (4.6 for Profile B, 4 for Profile C), the depth calculated at Profile B yields a depth of 2.892×4.6=13.3 km, while Profile C yields a value of 2.892×4=11.6 km.

Profile A gives a more ambiguous result, which seems in between the behaviour of f^{HC} and f^{VC} (Vertical Cylinder) considering the MWCS evolution across the three wavelet families. If we consider the anomaly to be generated predominantly by a homogeneous structure that is of Horizontal Cylinder type, the depth of its core would correspond to a scale of ~5.6, yielding a value of 2.892×5.6=16.2 km. If we consider rather a Vertical Cylinder type, the top of the corresponding dike would be located at a depth of 2,892×4=11.6 km.

This would suggest a cylindrical structure which core is dipping westwards, at the depths mentioned above, and located below the Uinta Mountains. As we move westwards, the structure dips and possibly becomes more complex. Furthermore, the dipping renders it less predominant in the Bouguer anomaly produced, which can allow other shallower structures to modify the overall signal shape, rendering its analysis more difficult. We now discuss the geological relevancy of such structure.

4.3 GEOLOGICAL INTERPRETATION

Our findings are consistent with the surface geology since our gravity map shows a relatively good correlation with the geological map (Fig. 5(a)). Negative anomalies are found in the Uinta and Wyoming basins, where relatively less dense Mesozoic and Cenozoic sediments deposited. Positive anomalies are found along the trace of the Uinta pop-up, striking E-W, where Proterozoic sediments are exposed. These results are similar to those described by (Behrendt and Thiel, 1963) and (Khatun, 2008).

Moreover, the depth calculation for the body causing the main positive anomaly provides depths consistent with previous works. For example, (Prodehl and Lipman, 1989), using seismic data, identified relatively high P-wave velocities, in the middle crust from 10 to 20 km depth, below the Flaming Gorge, northeast of the Uinta Mountains. These depths correspond to the depths obtained with our method (from 11 to 16km). Prodhel and Lipman (1990) assumed that these high velocities may be related to a relatively dense middle crust, within a thick crust, up to 40 km thick (Bashir et al., 2011). Khatun (2008) produced residual Bouguer anomaly map of the Uinta Mountains showing that the major positive anomaly below the Uinta Mountains may be located from 0 to 25 km depth. The interpretative cross-sections built by Khatun (2008) also show a relatively dense body in the core of the Uinta Mountains.

Three different hypotheses that explain the cylindrical gravity anomaly, dipping westward from ~11 to 16 km, may be considered based on the geological settings of the Uinta Mountains and previous works:

The first hypothesis is to infer the presence of different rounded batholiths of mantle-derived basaltic magma, aligned along the core of the Uinta pop-up. The presence of such batholiths is supported by the presence of igneous Cenozoic rocks at the surface in the Uinta Mountains. If batholiths were ascending higher to the east, coalescing spherical batholiths may produce the positive cylindrical gravity anomaly, dipping westward.

The second hypothesis is to infer the presence of a dense middle crust, as described by Prodehl and Lipman (1990) below the Flaming Gorge, partially involved in the core of the Uinta Mountains pop-up. The cross-section across the Uinta Mountains of Gries (1983) shows a pop-up structure with thrusts reaching depth up to 8 km. Assuming that these thrusts may reach the relatively dense middle crust, a part of this dense body may be involved in the core of the pop-up. If the core is slightly dipping westward, such configuration may also produce the positive cylindrical gravity anomaly.

The third hypothesis is related to the presence of the Cheyenne Suture below the Uinta Mountains, as described by (Crosswhite and Humphreys, 2003). Suture areas are commonly associated with high-density rocks, commonly ophiolites in eclogite or blue-schist facies, associated with the metamorphism of the subducting slab. During the formation of the suture, some parts of the high-density rocks maybe preserved at depth in the suture area. In this case, an elongated slice of such material, following the axis of the Uinta pop-up may be also a good candidate that explains the positive cylindrical gravity anomaly.

Moreover, there is probably a contribution of shallower rocks, above the main dense body that account for the positive cylindrical gravity anomaly. These rocks may correspond to the relatively dense quartzite of the Uinta Mountains Group (Khatun, 2008).

CONCLUSIONS

In this paper we have introduced a new method of interpreting Continuous Wavelet Transform diagrams for the analysis of Potential Field data. Wavelets, inspired by source functions, whose Fourier transform can be rewritten in terms of modified Bessel functions of second kind, yield an empirical law. We have verified the empirical law on various source types and derivative orders, linking directly the MWCS to the source depth, with a dependence on the Bessel functions orders. A demonstration of the use of the law, using synthetic examples, shows that we can automatically determine the source characteristics without any prior knowledge. The method, thanks to its precision in analysing the signal shape, can be applied to structures that are well resolved, irrespective of the wavelet chosen.

The MWCS analysis was finally applied on the Uinta Mountains range, suggesting a horizontal cylinder-type structure, which core depth dips from ~11-16km westwards, which structure possibly becomes more complex and deeper further west. This correlates with previous findings and studies, and raise certain hypotheses about the crust structure in the area.

Such developments suggest wavelet methods can serve beneficially for subsequent inversion algorithms. Their implementations do not require *a-priori* knowledge, while yielding important information about source characteristics with physically based arguments. These observations suggest that the relatively expensive computational cost of the wavelet transform can be compensated partly by the richer information extracted from data, as well as the potentially re-usable results for inversion.

More generally, our results show that potential field data analysis can be approached advantageously from the spectral domain, in which parameters that are not obvious in real domain become clear and reveal essential information about the sources. This new knowledge, along with further developments such as the use of any arbitrary wavelet or synchro-squeezed transform, can offer new possibilities in Potential Field analysis in 1D and 2D contexts.

ACKNOWLEDGEMENTS

The lead author (P. Cavalier) acknowledges the Claude Leon Foundation for funding the project.

REFERENCES

Abdelrahman, E.M., 1989. Gravity interpretation using correlation factors between successive least-squares residual anomalies. Geophysics 54, 1614. doi:10.1190/1.1442629

Abdelrahman, E.M., Essa, K.S., 2015. Three Least-Squares Minimization Approaches to Interpret Gravity Data Due to Dipping Faults. Pure Appl. Geophys. 172, 427–438. doi:10.1007/s00024-014-0861-4

Archibald, N., Gow, P., Boschetti, F., 1999. Multiscale edge analysis of potential field data. Explor. Geophys. 30, 38. doi:10.1071/EG999038

Bashir, L., Gao, S.S., Liu, K.H., Mickus, K., 2011. Crustal structure and evolution beneath the Colorado Plateau and the southern Basin and Range Province: Results from receiver function and gravity studies. Geochemistry, Geophys. Geosystems 12, 1–18. doi:10.1029/2011GC003563

Behrendt, J.C., Thiel, E., 1963. A gravity and magnetic survey of the Uinta Mountains. J. Geophys. Res. 68, 857. doi:10.1029/JZ068i003p00857

Bird, P., 1998. Kinematic history of the Laramide orogeny in latitudes 35°–49°N, western United States. Tectonics 17, 780. doi:10.1029/98TC02698

Blakely, R., 1996. Potential theory in gravity and magnetic applications.

Burchfiel, Lipman, P., 1992. The Cordilleran orogen: conterminous US.

Cavalier, P., 2015a. On the Use of Maximum Wavelet Coefficient Scales in Potential Fields Analysis and Inversion, in: SAGA 14h Biennal Conference.

Cavalier, P., 2015b. Controlling Maximum Wavelet Coefficient Scales for Potential Field study, in: SEG Technical Program Expanded Abstracts 2015. Society of Exploration Geophysicists, pp. 1592–1595. doi:10.1190/segam2015-5848768.1

Cella, F., Fedi, M., Florio, G., 2009. Toward a full multiscale approach to interpret potential fields. Geophys. Prospect. 57, 543–557. doi:10.1111/j.1365-2478.2009.00808.x

Constenius, K.N., 1996. Late Paleogene extensional collapse of the Cordilleran foreland fold and thrust belt. Bull. Geol. Soc. Am. 108, 20–39. doi:10.1130/0016-7606(1996)108<0020:LPECOT>2.3.CO;2

Cooper, G.R.J., 2012. The semi-automatic interpretation of magnetic dyke anomalies. Comput. Geosci. 44, 95–99. doi:10.1016/j.cageo.2012.02.016

Cooper, G.R.J., 2006. Interpreting potential field data using continuous wavelet transforms of their horizontal derivatives. Comput. Geosci. 32, 984–992. doi:10.1016/j.cageo.2005.10.012

Crosswhite, J. a., Humphreys, E.D., 2003. Imaging the mountainless root of the 1.8 Ga Cheyenne belt suture and clues to its tectonic stability. Geology 31, 669–672. doi:10.1130/G19552.1

Daubechies, I., Lu, J., Wu, H.-T., 2011. Synchrosqueezed wavelet transforms: An empirical mode decomposition-like tool. Appl. Comput. Harmon. Anal. 30, 243–261. doi:10.1016/j.acha.2010.08.002

DeCelles, P.G., 2004. American Journal of Science LATE JURASSIC TO EOCENE EVOLUTION OF THE CORDILLERAN. Am. J. Sci. 304, 105–168. doi:10.2475/ajs.304.2.105

Decelles, P.G., Lawton, T.F., Mitra, G., 1995. Thrust timing, growth of structural culminations, and synorogenic sedimentation in the type Sevier orogenic belt, western United States. Geology 23, 699–702. doi:10.1130/0091-7613(1995)023<0699:TTGOSC>2.3.CO;2

Dickinson, W.R., Klute, M.A., Hayes, M.J., Janecke, S.U., Lundin, E.R., McKITTRICK, M.A., Olivares, M.D., 1988. Paleogeographic and paleotectonic setting of Laramide sedimentary basins in the central Rocky Mountain region. Geol. Soc. Am. Bull. 100, 1023–1039.

English, J.M., Johnston, S.T., Wang, K., 2003. Thermal modelling of the Laramide orogeny: Testing the flat-slab subduction hypothesis. Earth Planet. Sci. Lett. 214, 619–632. doi:10.1016/S0012-821X(03)00399-6

Essa, K.S., 2007. Gravity data interpretation using the s-curves method. J. Geophys. Eng. 4, 204–213. doi:10.1088/1742-2132/4/2/009

Essa, K.S., 2007. A simple formula for shape and depth determination from residual gravity anomalies. Acta Geophys. 55, 182–190. doi:10.2478/s11600-007-0003-9

Fedi, M., 2007. DEXP: A fast method to determine the depth and the structural index of potential fields sources. Geophysics 72, I1–I11. doi:10.1190/1.2399452

Fedi, M., Cella, F., Quarta, T., Villani, a. V., 2010. 2D Continuous Wavelet Transform of potential fields due to extended source distributions. Appl. Comput. Harmon. Anal. 28, 320–337. doi:10.1016/j.acha.2010.03.002

Gries, R., 1983. North-south compression of Rocky Mountain foreland structures.

Gupta, O.P., 1983. A least-squares approach to depth determination from gravity data. Geophysics 48, 357–360.

Hansen, W.R., 1965. Geology of the Flaming Gorge area, Utah-Colorado-Wyoming.

Heller, P.L., Paola, C., 1989. The paradox of Lower Cretaceous gravels and the initiation of thrusting in the Sevier orogenic belt, United States Western Interior. Geol. Soc. Am. Bull. 101, 864–875.

Hintze, L.F., Willis, G.C., Laes, D.Y.M., Sprinkel, D.A., Brown, K.D., 2000. Digital geologic map of Utah: Utah Geological Survey Map 179DM. CD-Rom, scale 1.

Hornby, P., Boschetti, F., Horowitz, F.G., 1999. Analysis of potential field data in the wavelet domain. Geophys. J. Int. 137, 175–196. doi:10.1046/j.1365-246x.1999.00788.x

Keating, P., Pilkington, M., 2004. Euler deconvolution of the analytic signal and its application to magnetic interpretation. Geophys. Prospect. 52, 165–182. doi:10.1111/j.1365-2478.2004.00408.x

Khatun, S., 2008. An integrated geological and geophysical study of the Uinta Mountains, Utah, Colorado and a geophysical study on Tamarix in the Rio Grande River basin, West Texas. ProQuest.

Kingsbury-Stewart, E.M., Osterhout, S.L., Link, P.K., Dehler, C.M., 2013. Sequence stratigraphy and formalization of the Middle Uinta Mountain Group (Neoproterozoic), central Uinta Mountains, Utah: A closer look at the western Laurentian Seaway at ca. 750Ma. Precambrian Res. 236, 65–84. doi:10.1016/j.precamres.2013.06.015

Lines, L.R., Treitel, S., 1984. A review of least-squares inversion and its application to geophysical problems. Geophys. Prospect. 32, 159–86.

Mallat, S., 1999. A Wavelet Tour of Signal Processing, A Wavelet Tour of Signal Processing. doi:10.1016/B978-012466606-1/50004-0

McMillan, M.E., Heller, P.L., Wing, S.L., 2006. History and causes of post-Laramide relief in the Rocky Mountain orogenic plateau. Bull. Geol. Soc. Am. 118, 393–405. doi:10.1130/B25712.1

Moreau, F., Gibert, D., Holschneider, M., Saracco, G., 1999. Idenfitication of sources of potential fields with the continuous wavelet transform: basic theory. J. Geophys. Res. 104, 5003–5013.

Moreau, F., Gibert, D., Holschneider, M., Saracco, G., 1997. Wavelet analysis of potential fields. Inverse Probl. 13, 165–178.

Nabighian, M.N., 1972. The analytic signal of two dimensional magnetic bodies with polygonal cross section: its properties and use for automated anomaly interpretation. Geophysics 37, 507–517. doi:10.1190/1.1440276

Ouadfeul, S., Aliouane, L., 2012. Multiscale Analysis of Geophysical Signals Using the 2D Continuous Wavelet Transform, in: Baleanu, D. (Ed.), Wavelet Transforms and Their Recent Applications in Biology and Geoscience.

Paulsen, T., Marshak, S., 1999. Origin of the Uinta recess, Sevier fold-thrust belt, Utah: Influence of basin architecture on fold-thrust belt geometry. Tectonophysics 312, 203–216. doi:10.1016/S0040-1951(99)00182-1

Prodehl, C., Lipman, P., 1989. Crustal Structure of the Rocky Mountain region Geological, 1–37. doi:10.1130/MEM172-p249

Reid, A.B., Allsop, J., Granser, H., Millett, A., Somerton, I., 1990. Magnetic interpretation in three dimensions using Euler deconvolution. Geophysics 55.

Reid, A.B., Ebbing, J., Webb, S.J., 2014. Avoidable Euler Errors - the use and abuse of Euler deconvolution applied to potential fields. Geophys. Prospect. 62, 1162–1168. doi:10.1111/1365-2478.12119

Roshandel Kahoo, A., Nejati Kalateh, A., Salajegheh, F., 2015. Interpretation of gravity data using 2-D continuous wavelet transformation and 3-D inverse modeling. J. Appl. Geophys. 121, 54–62. doi:10.1016/j.jappgeo.2015.07.008

Roy, M., Jordan, T.H., Pederson, J., 2009. Colorado Plateau magmatism and uplift by warming of heterogeneous lithosphere. Nature 459, 978–982. doi:10.1038/nature08052

Sailhac, P., Gibert, D., Boukerbout, H., 2009. The theory of the continuous wavelet transform in the interpretation of potential fields: a review. Geophys. Prospect. 517–525. doi:10.1111/j.1365-2478.2009.00794.x

Salem, A., Ravat, D., Smith, R.S., Ushijima, K., 2005. Interpretation of magnetic data using an enhanced local wavenumber (ELW) method. Geophysics 70, 7–12.

Sprinkel, D.A., 2014. The Uinta Mountains. Utah Geol. Surv. Notes 46, 1–4.

Stone, D.S., 1993. Tectonic Evolution of the Uinta Mountains: Palinspastic Restoration of a Structural Cross Section Along Longitude 109° 15,́ Utah. Utah Geological Survey.

Thompson D.T., 1982. Euldph: A new technique for making computer assisted depth estimates from magnetic data. Geophysics 47, 31–37.

Weil, A.B., Yonkee, W.A., 2012. Layer-parallel shortening across the Sevier fold-thrust belt and Laramide foreland of Wyoming: Spatial and temporal evolution of a complex geodynamic system. Earth Planet. Sci. Lett. 357-358, 405–420. doi:10.1016/j.epsl.2012.09.021

Wolfram Research, Inc., Mathematica, Version 10.4, Champaign, IL (2016).

Cook, K.L, Bankey, V., Mabey, D.R., DePangher, M., 1990, Utah Bouguer Gravity Grid, U.S. Geological Survey: U.S. Dept. of Interior, EROS Data Center